LANGMUIR Article
Cite This: Langmuir 2019, 35, 7396−7404
pubs.acs.org/Langmuir

Polymeric Nanoparticles Limit the Collective Migration of Cellular Aggregates

Grégory Beaune,[†] Usharani Nagarajan,[†] Françoise Brochard-Wyart,[‡,§] and Françoise M. Winnik*[,†,∥,⊥]

[†]International Center for Materials Nanoarchitectonics (MANA), National Institute for Materials Science, 1-1 Namiki, Tsukuba, Ibaraki 305-0044, Japan

[‡]Sorbonne Université, UMR 168, Institut Curie, 26 rue d'Ulm, 75248 Paris, Cedex 05, France

[§]CNRS, UMR 168, Institut Curie, 26 rue d'Ulm, 75248 Paris, Cedex 05, France

[∥]Department of Chemistry, University of Montreal, CP 6128 Succursale Centre Ville, Montreal QC H3C3J7, Canada

[⊥]Department of Chemistry, University of Helsinki, FI-00014 Helsinki, Finland

Supporting Information

ABSTRACT: Controlling the propagation of primary tumors is fundamental to avoiding the epithelial to mesenchymal transition process leading to the dissemination and seeding of tumor cells throughout the body. Here we demonstrate that nanoparticles (NPs) limit the propagation of cell aggregates of CT26 murine carcinoma cells used as tumor models. The spreading behavior of these aggregates incubated with NPs is studied on fibronectin-coated substrates. The cells spread with the formation of a cell monolayer, the precursor film, around the aggregate. We study the effect of NPs added either during or after the formation of aggregates. We demonstrate that, in both cases, the spreading of the cell monolayer is slowed down in the presence of NPs and occurs only above a threshold concentration that depends on the size and surface chemistry of the NPs. The density of cells in the precursor films, measured by confocal microscopy, shows that the NPs stick cells together. The mechanism of slowdown is explained by the increase in cell−cell interactions due to the NPs adsorbed on the membrane of the cells. The present results demonstrate that NPs can modulate the collective migration of cells; therefore, they may have important implications for cancer treatment.

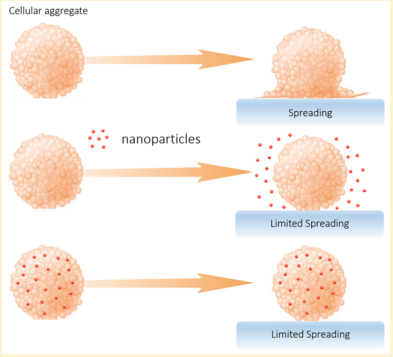

INTRODUCTION

Several recent in vivo studies, supported by in vitro mechanistic data, indicate that, inherently, gold nanoparticles (AuNP) are able to suppress or reduce the epithelial to mesenchymal transition (EMT) of tumor cells, a key process leading to cancer metastasis.[1] Nanoparticles tested in these studies include citrated gold nanospheres (AuNPs), 5 to 20 nm in diameter,[2] used by Arvizo et al. against epithelial ovarian cancer tumors, and 50-nm-long gold nanorods (AuNRs) coated with serum proteins shown by Zhou et al. to reduce the metastatic ability of human breast cancer cells.[3] The studies carried out in vivo and in vitro on isolated cells indicate that spherical AuNPs inhibit the proliferation of cancer cells by rescinding MAPK signaling and reverse EMT by up-regulating E-cadherin and reducing the secretion of proteins implicated in EMT.[2] Similarly, in vitro studies indicate that protein-coated AuNRs inhibit the migration and invasion of metastatic cancer cells by rescinding several energy-generation pathways and the subsequent impairment of F-actin.[3] In vivo assays confirmed the AuNR-induced reduction of cancer cell migration.[3] These important developments, which suggest new approaches to the treatment of metastasis,[4] were foreseen several years ago by researchers studying the effects of NPs on the migration of isolated cell. Yang et al. reported the inhibiting effect of spherical gold nanoparticles on the migration of isolated prostate carcinoma cells.[5] Tay et al. observed that titania, silica, and hydroxyapatite slow down the migration of epithelial cells assembled in 2D sheets and significantly compromise their wound healing capability by disrupting the intracellular microtubule assembly.[6] Earlier work by Zhang et al. indicated that the mobility of isolated primary human dermal fibroblasts was impaired by the addition of silica NPs (50 and 500 nm in size) via inhibition of the mRNA expression of adhesion-relevant genes.[7]

Given that liposomes and polymeric nanoparticles are used clinically as drug-delivery vehicles and extensively evaluated for future treatments in oncology, it is important to assess their intrinsic ability to affect cancer metastasis, a property that has been largely ignored in the past. This question is addressed in the study reported here, where we assess the effect of particles on the spreading of cellular aggregates, often used to model tissues and cancerous tumors.[8] Cellular aggregates were

Special Issue: Interfaces and Biology 1: Mechanobiology and Cryobiology

Received: May 25, 2018
Revised: July 4, 2018
Published: July 5, 2018

deposited on a substrate immersed in culture medium supplemented with particles. The extent of spreading of the aggregates was monitored by bright-field optical microscopy over several days. In addition, we performed similar spreading experiments with hybrid cell/particle aggregates formed by the treatment of cells with nanoparticles prior to aggregation. As model particles, we focused on fluorescently labeled polystyrene particles surface-modified with either carboxylate or amine groups to provide an anionic or cationic particle surface, respectively. Their diameter ranged from 20 to 1000 nm. This set of particles allows for a comparison of particles with the same composition but opposite surface charges and different sizes. We monitored the particle internalization in cells by confocal fluorescence microscopy.

To gain mechanistic insight into the phenomena observed, we discuss them within the framework of wetting dynamics. The spreading of cell aggregates results from the competition between cell−cell (W_{CC}) and cell−substrate (W_{CS}) adhesion[9,10] characterized by the spreading parameter $S = W_{CS} - W_{CC}$. If S is positive, then aggregates spread with the formation of a precursor film. The spreading dynamics result from the balance of the driving forces due to motile cells at the periphery of the film and the friction forces associated with the entry of cells from the aggregates into the film.[11,12] It is found both theoretically and experimentally that the area A of the spreading film increases with time t as $A = V^*R_0t$, where $V^* = S/\eta$ (with η being the bulk viscosity of cell aggregates) is the typical spreading velocity. The law of spreading is diffusive with a diffusion coefficient of $D = V^*R_0$ proportional to the radius of the aggregate R_0 and to the velocity V^*. Our aim is to study here how V^* is modified by the incorporation of the nanoparticles.

EXPERIMENTAL SECTION

Materials and Methods. Water (18.2 MΩ·cm) was deionized using a Milli-Q water purification system (Millipore). The fluorescent polystyrene particles (FluoSpheres) were purchased from Invitrogen. Their diameters, provided by the supplier, were 20 nm (carboxylated polystyrene, Carbo20, F8786), 200 nm (carboxylated polystyrene, Carbo200, F8810), 1 μm (carboxylated polystyrene, Carbo1000, F8821), and 200 nm (amino-polystyrene, Amine200, F8763). Particles were labeled with a proprietary dye (λ_{max}= 580 nm, $\lambda_{max,\,fl}$ = 605 nm). Dulbecco's Modified Eagle's Medium (DMEM, Life Technologies Co.), antibiotics (100 μg/mL streptomycin and 100 U/mL penicillin, Life Technologies Co.), and trypan blue 0.4 wt % were obtained from Life Technologies Co. Fetal bovine serum (FBS, Sigma-Aldrich Co.) and fibronectin were purchased from Sigma-Aldrich, bovine serum albumin (BSA) was purchased from Wako Co., Triton X-100 solution was purchased from MP Biomedicals Co., anti-α-tubulin mouse IgG1 antibody (A11126) and DAPI were purchased from Molecular Probes, and Alexa 405 antigoat antibody (ab175664) was purchased from Abcam Co.

Dynamic light scattering (DLS) and zeta-potential measurements were performed on a Beckman Coulter Delsa Nano system at a temperature of 20 °C using particle suspensions in PBS at pH 7.4. Their concentrations were Carbo20, 8.6 pmol/L; Carbo200, 1.5×10^{-2} pmol/L; Carbo1000, 9×10^{-5} pmol/L; and Amine200, 1.5×10^{-2} pmol/L. The Smoluchowski approximation was used to convert the electrophoretic mobility to zeta potentials.

Fibronectin-coated glass substrates were prepared starting with 25 mm circular glass coverslips precleaned by sonication in ethanol for 5 min, drying at room temperature, and exposure to deep UV for 10 min. They were coated with fibronectin by drop casting (Sigma-Aldrich) with a fibronectin solution (100 μg/mL) in PBS (pH 7.4) for 45 min at room temperature. The coverslips were rinsed with PBS (pH 7.4) and used in aggregate spreading experiments.

Cell Culture and Aggregate Preparation. WT mouse colon carcinoma CT26 cells stably transfected with LifeAct-GFP were used throughout the study. They were a generous gift from Dr. Danijela Vignjevic (UMR 144, Institut Curie, France). Cells were cultured at 37 °C under a 95% air/5% CO_2 atmosphere in culture medium consisting of DMEM supplemented with 10% (v/v) FBS and antibiotics (100 μg/mL streptomycin and 100 U/mL penicillin). Upon reaching confluence, cells were detached from the flask using trypsin and dispersed in DMEM. They were recovered and used to prepare aggregates by the hanging droplet method.[13,14] Droplets (15 μL) of culture medium containing cells were deposited on the lid of a Petri dish. The lid was inverted and placed on top of a Petri dish filled with PBS such that the droplets containing the cells in the medium and hanging from the lid were maintained under a high-humidity atmosphere. Because of gravity, cells fall to the bottom of the droplets, and because of N-cadherin expression on the cell membrane, the cells start to adhere to each other. Aggregates were obtained after a 3-day incubation at 37 °C under a 95% air/5% CO_2 atmosphere. For hybrid cell/NP aggregates, the same protocol was followed except that NPs were added to the cell suspension after dispersion of the cells in DMEM to reach the desired concentration. To remove the excess particles left in suspension around the hybrid aggregate, the medium was changed gently after fixation of the aggregates to the substrate (30 min). The spreading experiments were recorded immediately after the medium exchange.

Several volume fractions were defined in the study. In the case of cell aggregates exposed to NPs, we define

$$\Phi = \frac{\text{total volume of NPs in the observation chamber}}{\text{total volume of medium in the observation chamber}}$$

In the case of hybrid cell−NPs aggregates, we use two volume fractions. Φ is defined as

$$\Phi = \frac{\text{total volume of NPs in one droplet}}{\text{total volume of medium in one droplet}}$$

with a droplet here referring to the hanging droplet method. The second volume fraction is F, defined as

$$F = \frac{\text{total volume of NPs}}{\text{total volume of NPs} + \text{total volume of cells}}$$

It has to be noticed that F corresponds to the initial situation in the droplets when cells and NPs are mixed together.

Aggregate Spreading Visualized by Bright-Field Microscopy. For the observation of cell aggregates deposited in observation chambers containing NPs, the chambers consisted of a fibronectin-coated glass coverslip placed in a magnetic imaging chamber (Chamlide CMB, CM-B25-1) filled with a CO_2-equilibrated culture medium. An aliquot of a suspension of particles in the culture medium with the desired volume fraction was placed in the chamber and homogenized. After a few minutes, cell aggregates were deposited randomly on the substrate. For this type of experiment, the maximum volume fraction Φ was $\sim 10^{-4}$ since samples of higher Φ values were very opaque and aggregates could not be observed by bright-field microscopy. (b) Observation of hybrid cell/NP aggregates deposited in a medium without NP_S: the same protocol was followed except that NPs were not added to the magnetic chamber because they were already inside aggregates. Here, contrary to the previous case where Φ was limited by the transparency of the sample, there is no limitation of Φ in the hanging droplet.

For all conditions, the final volume in the chamber was 1.5 mL, and the chamber was sealed with mineral oil to prevent evaporation of the buffer. Aggregate spreading was observed using an inverted microscope (TIRF AF 6000LX, Leica) equipped with a 10× 0.30 NA objective. Videos were recorded with a CCD camera (Photometrics Cascade 512B, Roper Scientific) at an acquisition rate of 1 frame/10 min. Images were exported from the instrument software in TIFF format and visualized using ImageJ software package v.1.46r (National Institutes of Health, Bethesda, MD).

DOI: 10.1021/acs.langmuir.8b01736
Langmuir 2019, 35, 7396−7404

Aggregate Spreading Visualized by Confocal Fluorescence Microscopy. Cell aggregates, formed without NPs, were deposited randomly on a fibronectin-coated glass coverslip placed in a magnetic imaging chamber filled with CO_2-equilibrated culture medium, followed by the addition of a particle suspension when necessary. Chambers were kept for 20 h in an incubator (37 °C under a 95% air/5% CO_2 atmosphere). Subsequently, the aggregates were fixed and stained as follows. Cells were fixed in 4% paraformaldehyde (PFA)-PBS for 15 min and then rinsed with PBS. They were cooled on ice, permeabilized, and blocked for 15 min with a BSA-Triton solution (1% BSA, 0.1% Triton X-100 in PBS). They were rinsed three times for 5 min with PBS (pH 7.4). For tubulin staining, aggregates were treated with a primary antibody (anti-α-tubulin mouse IgG1 antibody, A11126, Molecular Probes) in a dilution of 1/100 by volume in 1% BSA-PBS solution for 1 h at room temperature. The chamber was rinsed three times with PBS. The aggregates were treated for 1 h with either DAPI or Alexa 405 antigoat antibody diluted 1/500 and 1/100, respectively, in 1% BSA-PBS. Finally, the chamber was placed on a shaker, and the aggregates were rinsed three times with PBS for 15 min. The PBS solution was removed, and the aggregates were protected against photobleaching with a slow antifade reagent in glycerol/PBS (S2828, Invitrogen). The stained aggregates were observed with an inverted confocal microscope (TCS SP5, Leica Microsystems) equipped with a 10× 0.30 NA objective and a 63× 1.4 NA objective with oil immersion. Images were exported from the instrument software in TIFF format and visualized using ImageJ software package v.1.46r (National Institutes of Health, Bethesda, MD). The same protocol was applied starting with hybrid cell/NP aggregates but omitting the addition of a particle suspension.

Toxicity Assay. Viability tests with trypan blue were performed on cell aggregates incubated in DMEM for 20 h on substrates coated with fibronectin.

The following systems were studied: (i) CT26 cell aggregates incubated for 20 h with a suspension of particles added in volume fractions Φ of 6.8×10^{-5} in the cases of Carbo200 and Amine200, 2.6×10^{-4} in the case of Carbo20, and 4.2×10^{-5} in the case of Carbo1000 and (ii) hybrid cell/NP aggregates incubated for 20 h in a medium without NPs. The type and volume fraction of NPs used for the formation of aggregates were Carbo20 with $\Phi = 3.4 \times 10^{-3}$ ($F = 0.77$), Carbo200 with $\Phi = 1.8 \times 10^{-6}$ ($F = 4 \times 10^{-3}$), Amine200 with $\Phi = 1.8 \times 10^{-5}$ ($F = 1.8 \times 10^{-2}$), and Carbo1000 with $\Phi = 4.2 \times 10^{-4}$ ($F = 0.40$).

After incubation, a solution of trypan blue was added to the experimental chamber to reach a final concentration of 0.1 wt %. After 10 min, the trypan blue solution was removed and replaced with PBS. Micrographs were recorded with a bright-field microscope (DMIL-TR/EC3, Leica Microsystems microscope equipped with 10× 0.3 NA and 20× 0.5 NA objectives) in order to count the dead cells (blue) among the colorless live cells. Very few dead cells were detected in the precursor film formed around the aggregates without particles or with them (Figure S4).

Image Analysis. The area of the precursor film, A, was determined from the perimeter of the film drawn by hand on each bright-field micrograph. The radius R_0 of the aggregate was calculated from A_0 assuming that the aggregate is a spherical cup. The velocity field in a cell monolayer was mapped by PIV analysis. Stacks of images were analyzed by using the MatPIV software package for MATLAB (The MathWorks, Natick, MA)[15] as previously described in ref 16. The subwindow size was 18 μm, and the delay between successive images was 10 min.

Cell Densities of Precursor Films. Cell aggregates were formed, and then spreading experiments were performed (as described before) without NPs or with Carbo20 with $\Phi = 6.8 \times 10^{-6}$ or with Carbo20 with $\Phi = 6.8 \times 10^{-4}$. After 20 h, aggregates were observed with the confocal microscope mentioned previously in bright-field mode. The surface density of cells in the films was calculated as follow: surface density = number of cells in the film/$(A_{(t=20\ \mathrm{h})} - A_0)$. Calculations were performed on 11, 6, and 10 aggregates for $\Phi = 0$, 6.8×10^{-6}, and 6.8×10^{-4}, respectively. Cells were counted manually, and areas were measured with ImageJ.

Stastistical Analysis. The statistical analysis of the spreading velocities was performed using the Student t test on the values of V^*. A p-value smaller than or equal to 0.05 was considered to be significant.

RESULTS AND DISCUSSION

In this section, we give the physical properties of the particles and present the results of experiments where we monitor the effects of particles on the spreading of aggregates. We consider first situations in which cell aggregates are treated with particles and allowed to spread on a substrate. Second, we record the spreading of hybrid cell/particle aggregates obtained by mixing particles and isolated cells before initiating the aggregation process.

Characterization of the Particles. The set of assessed particles includes three samples of carboxylated polystyrene particles, 20, 200, and 1000 nm in diameter, and a sample of aminated polystyrene particles with a diameter of 200 nm. The particles were selected in view of their surface charge, size, size distribution, stability in aqueous media, ready availability, and low toxicity to cells.

The hydrodynamic diameter (d_h) and zeta potential of the particles in aqueous phosphate-buffered saline (PBS) are listed in Table 1, where we refer to the samples as Carbo20, Carbo200, Carbo1000, and Amine200. In this nomenclature, the prefix refers to the surface functionality of the particles and the number indicates the approximate diameter of the particles. Preliminary studies by asymmetrical flow field−flow fractionation (AF4)[17] indicate that the particles do not aggregate massively in cell culture medium (DMEM) with or without FBS (10%). The hydrodynamic diameter of carboxylated particles increased by ca. 10 nm in DMEM supplemented with FBS, presumably due to the adsorption of serum proteins. The aminated particles formed loose agglomerates of ∼1 μm hydrodynamic diameter in FBS-containing DMEM.

Table 1. Particle Diameter (d_{TEM})[a], Hydrodynamic Diameter (d_h), and Zeta Potential (ZP) of the Particles Suspended in PBS pH 7.4[b]

	supplier-provided diameter	hydrodynamic diameter	zeta potential
sample	d_{TEM} (nm)	d_h (nm)	ZP (mV)
Carbo20	24 ± 3	49 ± 1	−37.2 ± 2.5
Carbo200	200 ± 6	218 ± 2	−35.9 ± 1.3
Carbo1000	1100 ± 36	881 ± 136	−53.3 ± 2.7
Amino200	200 ± 11	296 ± 19	0.8 ± 0.5

[a]Provided by the supplier. [b]Concentration in the Experimental Section.

Spreading of Cell Aggregates Exposed to NPs. *Area of the Precursor Film.* When CT26 cell aggregates are deposited on a fibronectin-coated substrate, they spread by forming a cell monolayer, the precursor film, that expands around the aggregate. The process is illustrated in Figure 1A, which presents optical micrographs recorded immediately after the aggregate deposition (time 0) and after 5, 10, and 15 h of spreading. The blue trace in each micrograph follows the contour of the precursor film. It delineates the spreading area, A, of the aggregate at each time point. The area increases significantly as time elapses. Figure 1B presents micrographs recorded during the spreading of a CT26 cell aggregate exposed, at time 0, to a suspension of Amine200 NPs (volume

DOI: 10.1021/acs.langmuir.8b01736
Langmuir 2019, 35, 7396−7404

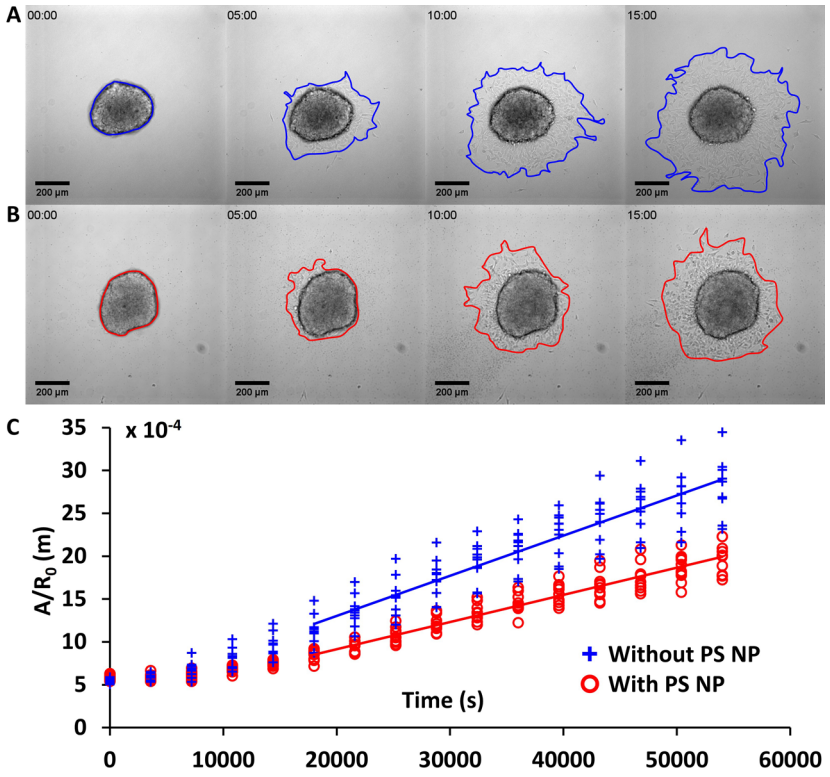

Figure 1. Spreading of aggregates on fibronectin-coated glass coverslips observed in bright field (A) without the addition of NPs as a reference and (B) with the addition of amine-coated NPs (Amine200, $\Phi = 6.8 \times 10^{-6}$). Contact areas A are defined by areas enclosed by blue and red contours, respectively. (C) Time evolution of the monolayer area of spreading aggregates normalized by the initial aggregate radius R_0. Blue and red markers correspond to the case without and with the addition of NPs, respectively. Each condition corresponds to 10 aggregates, and the solid lines correspond to the average of the 10 aggregates.

fraction $\Phi = 6.8 \times 10^{-6}$). For each time point, the spreading area, delineated by the red trace, is smaller than in the corresponding control experiment (Figure 1A). Figure 1C shows the evolution with time of the areas A of 10 aggregates in the case of aggregates treated with Amine200 NPs (red circles) and the control measurements (blue crosses). The areas were determined precisely from the micrographs and normalized by the initial aggregate radius (R_0). The red and blue lines drawn in Figure 1C represent fits of the data sets to the diffusive law (eq S2) derived from a theoretical model of the spreading of cell aggregates briefly described in the SI.

Aggregate Spreading Velocity. The slopes of the fitted A/R_0 straight lines correspond to the average spreading velocity (V^*) of aggregates (eq S2). They are $(3.2 \pm 0.4) \times 10^{-8}$ and $(4.7 \pm 0.5) \times 10^{-8}$ m/s for the Amine200-treated aggregates and the control, respectively. Hence, the presence of Amine200 NPs ($\Phi = 6.8 \times 10^{-6}$) induces a decrease of nearly 30% in the aggregate spreading velocity compared to the control. The spreading velocity of cell aggregates varies as a function of the volume fraction of the particles, Φ. The profile of V^* vs particle concentration is the same for all particles: V^* remains constant up to a threshold particle volume fraction Φ_e^*, beyond which V^* decreases by ~30% (Figure 2) when Φ_e^* reaches the value beyond which the samples lose their transparency. Measurements with suspensions of $\Phi \gtrsim 2 \times 10^{-4}$ were impossible since the suspensions were opaque and masked the aggregates in the bright-field optical micrographs. Φ_e^* is determined by taking the highest volume fraction before the decrease in V^*. The Φ_e^* value varies with the size of the particles as follows: $\Phi_e^*(\text{Carbo200}) < \Phi_e^*(\text{Carbo20}) < \Phi_e^*(\text{Carbo1000})$. The threshold values measured for suspensions of Carbo200 and Amine200 were identical ($\Phi_e^* = 1 \times 10^{-6}$), implying that the particle charge does not affect the spreading velocity. The cell density in the precursor film increases with NP concentration. For example, the cell density in the films increases from 135 to 177 cells/

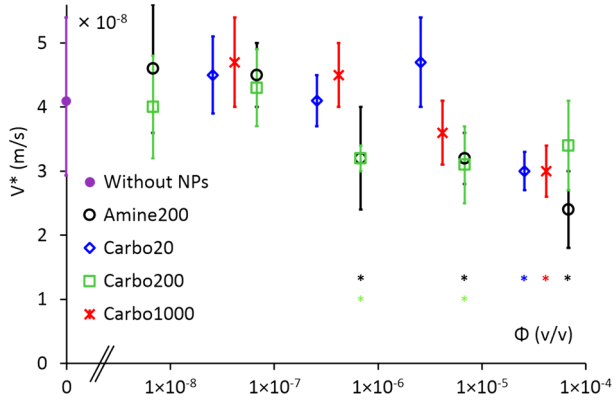

Figure 2. Spreading of cell aggregates exposed to NPs. Representation of the spreading velocity V^* as a function of the volume fraction of particles φ. Influence of the size and surface chemistry of NPs. Purple ● corresponds to aggregates without NPs, blue ◊ corresponds to Carbo20, green □ corresponds to Carbo200, black ○ corresponds to Amine200, and red × corresponds to Carbo1000. Each condition corresponds to 10 aggregates, and error bars represent the standard deviation. * Denotes $p < 0.05$ compared to the reference (without NPs) using the Student t test.

DOI: 10.1021/acs.langmuir.8b01736
Langmuir 2019, 35, 7396−7404

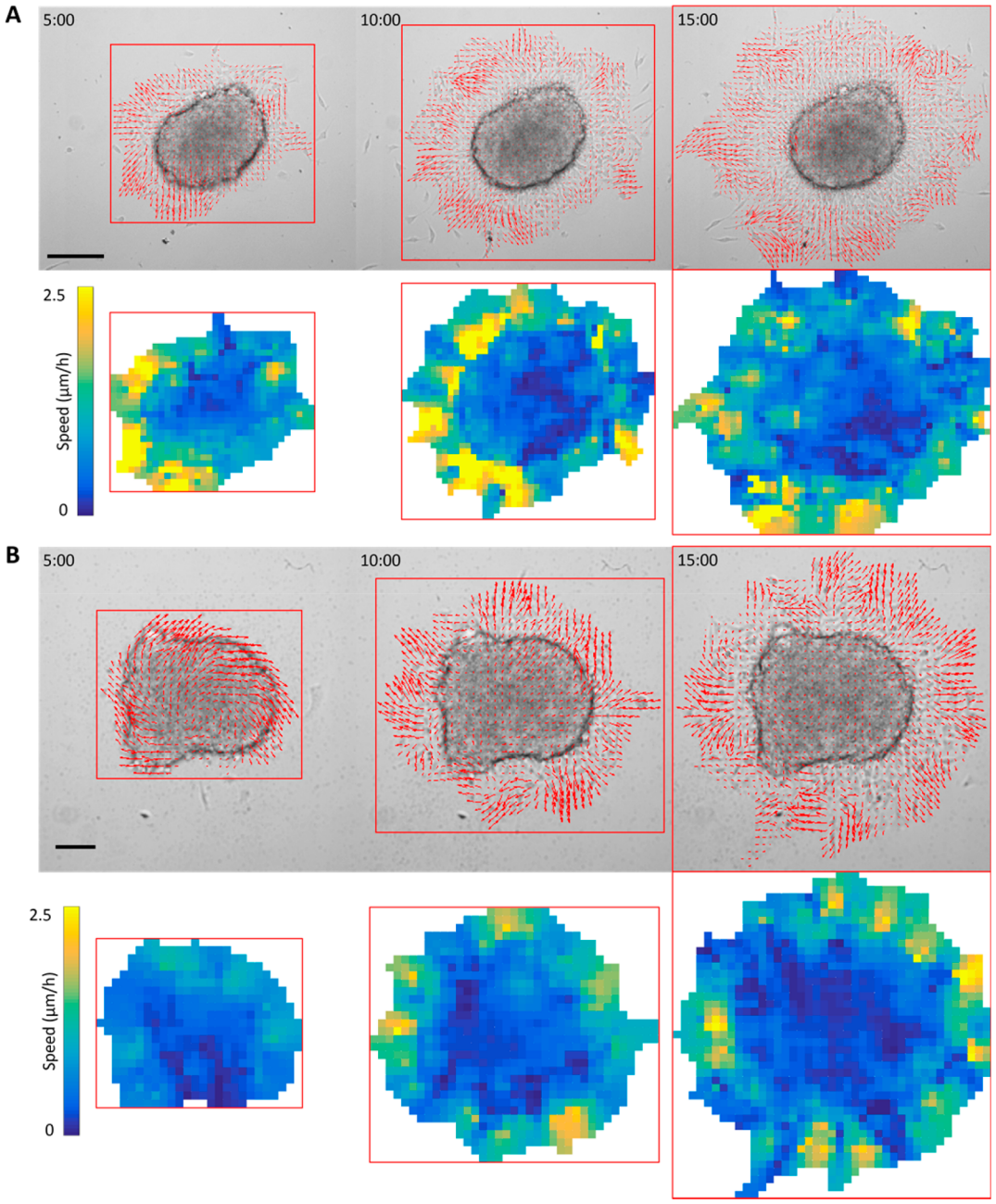

Figure 3. Spreading of aggregates on fibronectin-coated glass coverslips in bright-field microscopy at different times. No (A) NPs and (B) Amine200 with $\Phi = 1.8 \times 10^{-5}$ have been added to the cellular medium. Using the PIV method, (A and B top) the direction of velocity fields and (A and B bottom) the direction of heat maps show the spatial distribution of velocity fields. Scale bars represent 200 and 100 μm in each panel of (A) and (B), respectively.

mm^2 as the Carbo20 NP volume fraction increases from 0 to 2.6×10^{-4} (Figure S2).

The velocity field of cells in the precursor film was mapped by particle imaging velocimetry (PIV), a technique often used to evaluate cell migration.[18,19] Velocity maps drawn from micrographs recorded for the spreading of CT26 cell aggregates alone and in the presence of Amine200 particles are presented in Figure 2A,B, respectively, 5, 10, and 15 h after deposition. PIV maps provide the direction of the velocity fields (micrographs on the top row of Figure 2A,B), and heat maps show the spatial distribution of the velocity field (micrographs on the second row of Figure 2A,B). The velocity of the precursor film is radial in both cases, with long-range correlations of characteristic length ~60 μm, i.e., a few times the cell diameter. The amplitude of the velocity of the migrating cells is reduced for aggregates in the presence of particles, confirming the V^* data calculated from the area of the precursor film (Figure 5). PIV maps monitoring the spreading of cell aggregates treated with Carbo20, Carbo200, and Carbo1000 ($\Phi = 6.8 \times 10^{-5}$, 1.8×10^{-5}, and 4.2×10^{-6}, respectively) are presented in Figure S3. They exhibit the same trends as Amino200 particles: (1) the cells migrate radially from the aggregates and (2) the particles slow the spreading of cell aggregates by approximately 30%.

It is known that the motility of individual cells can be impaired as a consequence of the inherent toxicity of

DOI: 10.1021/acs.langmuir.8b01736
Langmuir 2019, 35, 7396−7404

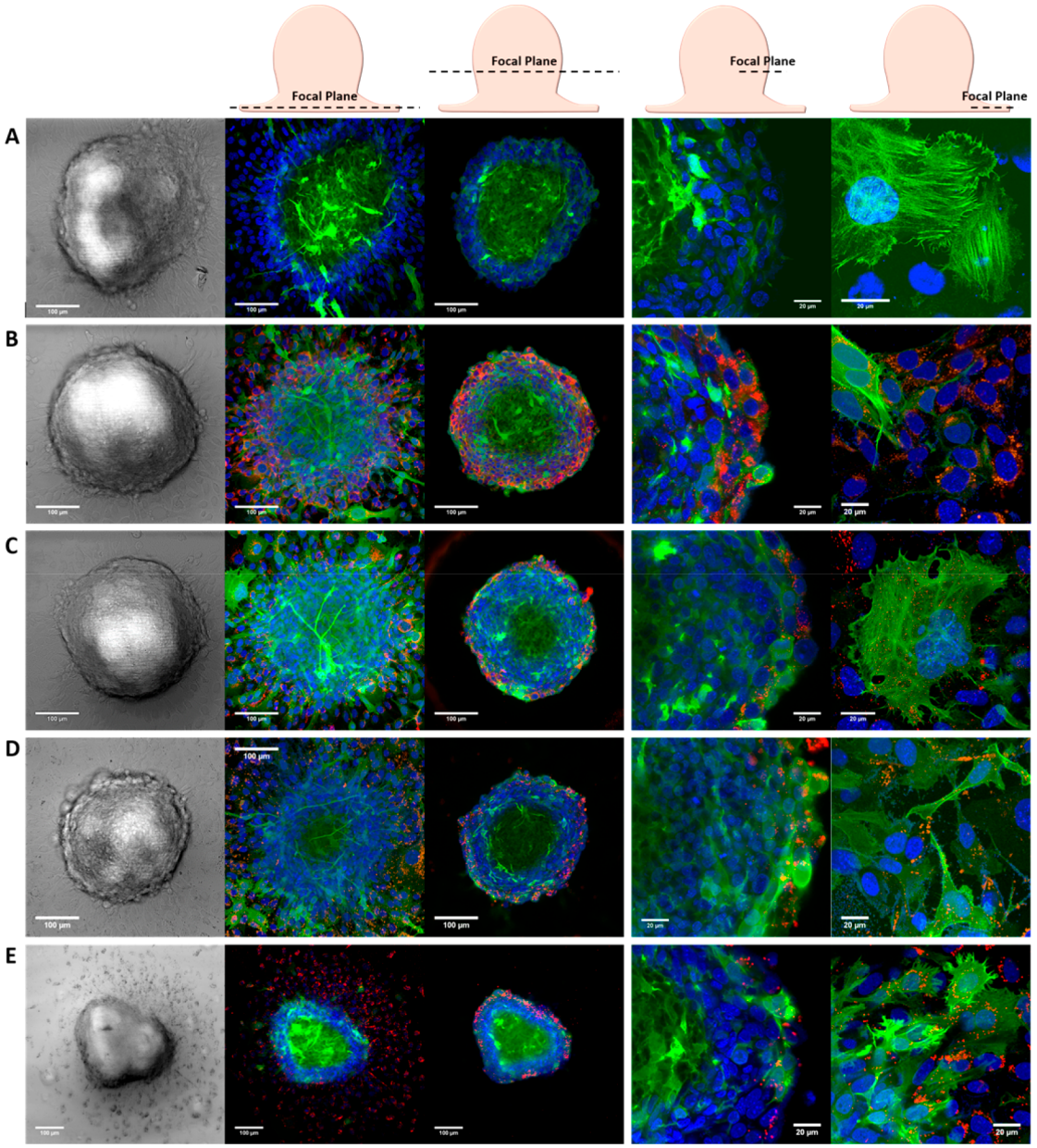

Figure 4. Spreading of cell aggregates incubated or not with particles for 20 h observed in bright-field microscopy and in confocal microscopy. Cell aggregates are observed (A) without the addition of NPs, after incubation with (B) Carbo20 with $\Phi = 2.6 \times 10^{-5}$, (C) Carbo200 with $\Phi = 6.8 \times 10^{-6}$, (D) Amine200 with $\Phi = 6.8 \times 10^{-6}$, and (E) Carbo1000 with $\Phi = 1.3 \times 10^{-5}$. F-actin is visible in green (cells are transfected with GFP), the particles are visible in red, and the nucleus is visible in blue (cells are stained with DAPI). Aggregates are observed in bright-field microscopy and in fluorescence microscopy on the surface of the substrate (observation of the aggregates with the precursor films) and above the substrate (observation of the aggregates without the precursor films).

nanoparticles.[20] Such effects were ruled out by assessing the toxicity of the particle samples used here. Aggregates, deposited on a substrate, were incubated for 20 h with each type of NP applied at volume fractions exceeding the threshold value (Carbo200 and Amine200, $\Phi = 6.8 \times 10^{-5}$; Carbo20, $\Phi = 2.6 \times 10^{-4}$; and Carbo1000, $\Phi = 4.2 \times 10^{-5}$). The trypan blue assay performed on the recovered aggregates indicated that the NPs do not significantly affect the viability of cells in the precursor film (Figure S4A–F).

Confocal Fluorescence Microscopy Imaging of the Spreading of Aggregates. Micrographs of aggregates treated with the various particles and allowed to spread for 20 h are presented in Figure 4. The CT26 cells employed were transfected with GFP to visualize the actin network (green emission) and stained with DAPI, a nucleus-targeted dye (blue emission). Particles were detected by their red emission (Figure 4) and applied at a concentration of 10 μg/mL (corresponding to $\Phi = 2.6 \times 10^{-5}$ for Carbo20, $\Phi = 6.8 \times 10^{-6}$ for Carbo200 and Amine 200, and $\Phi = 1.3 \times 10^{-5}$ for Carbo1000). At the end of the incubation, the medium was exchanged to remove the particles in excess. The resulting aggregates were imaged at several z values as depicted in Figure 4 (top). All particles penetrate the aggregate to some extent, as seen in the micrographs of the third column from the left, representing an image through the entire aggregate (precursor film excluded). The smallest particles (Carbo20,

DOI: 10.1021/acs.langmuir.8b01736
Langmuir 2019, 35, 7396–7404

row B) are concentrated in the external cell layers of the aggregate, but they are detected throughout the aggregate. Carbo200, Carbo1000, and Amine200 penetrate only the outermost layers (up to ~30 μm) of the aggregates, as observed on the micrographs in the fourth column from the left, which presents an extended view of the external layers of the aggregates. Micrographs from the fifth column from the left are focused on the precursor film surrounding the aggregate. Particles are seen in all films. Fluorescence micrographs presented in Figure S5 present further evidence that cell aggregates ingest particles as they spread in a substrate. It is not clear at this point if the decrease in spreading velocity observed results from the incorporation of particles within the aggregate. This question is addressed in the following section.

Spreading of Hybrid Cell/Particle Aggregates. We reported previously that it is possible to entrap particles within cell aggregates by adding NPs to the cell suspension used in the preparation of aggregates by the hanging drop method.[14] This protocol was used here to prepare hybrid cells/particles over a wide range of particle concentration, from $\Phi = 10^{-10}$ to 10^{-3} volume fraction corresponding to $F \approx 10^{-7}$ to 0.7. The overall range of NP volume fractions studied here is wider than in the case of the addition of particles to preformed aggregates, as measurements were not hampered by the opacity of the cell medium in highly concentrated suspensions. Hybrid cell aggregates obtained with the most concentrated NP suspensions, $\Phi > 10^{-4}$ ($F > 0.1$), were significantly smaller than control aggregates or hybrid aggregates produced with particle suspensions of low volume fractions, R_0 ranging from ~250 to ~50 μm. Confocal fluorescence microscopy imaging of hybrid aggregates formed with NPs of various volume fractions confirmed the successful entrapment of NPs within the aggregates (Figure S6). Trypan blue tests performed on hybrid cell/particle aggregates formed with particle volume fractions ranging from $\Phi \approx 10^{-6}$ to 10^{-3} indicated that the viability of the cells was maintained (Figure S4E–H).

The average spreading velocity, V^*, of the aggregates was determined from measurements of the spreading area A, described above. The particle concentration dependence of the V^* values recorded for all types of particles is presented in Figure 5. Two concentration regimes are observed. For low NP volume fractions ($\Phi < 10^{-6}$), the average spreading velocity remains constant. Its value ($\sim 4 \times 10^{-8}$ m/s) is similar to the average spreading velocity of cell aggregates without particles. For high NP volume fractions ($\Phi > 10^{-6}$), the spreading of the aggregates slows gradually until it stops completely, independently of the size of the particle (Carbo20, 200, and 1000). We observe a larger decrease of V^* in the case of hybrid aggregates, compared to the case of the addition of NPs to aggregates. This is most probably due to the fact that we were able to observe the spreading of hybrid aggregates containing NP of much higher concentrations without losing the transparency of the aggregate medium.

DISCUSSION

In general, the decrease in spreading velocity indicates a decrease in the spreading parameter S/η, where $S = W_{CS} - W_{CC}$. The fact that the dynamics are not affected below Φ_e^* implies that the NP internalization does not modify the cell migration. It has been previously reported that internalized NPs modify cell migration by disrupting or inhibiting cellular pathways, often leading to the impairment of the cytoskeleton.[2−7] To assess if the polystyrene NPs employed here can

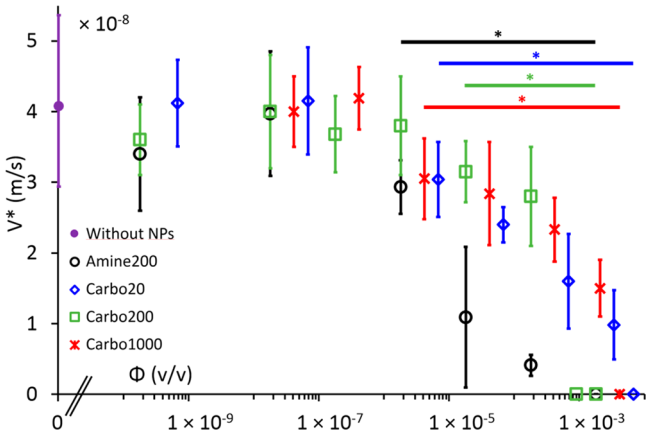

Figure 5. Representation of the spreading velocity of aggregates formed with NPs deposited on fibronectin-coated glass coverslips as a function of particle concentration. Influence of the size and surface chemistry of NPs. Purple ● corresponds to aggregates without NPs, blue ◊ corresponds to Carbo20, green □ corresponds to Carbo200, black ○ corresponds to Amine200, and red × corresponds to Carbo1000. * Denotes $p < 0.05$ compared to the reference (without NPs) using the Student t test.

affect the microtubules of cells, we carried out additional cell aggregate spreading experiments whereby aggregates were incubated with NPs for 20 h and immunolabeled for α-tubulin, one of the constituents of microtubules. Fluorescence microscopy observations were performed for aggregates treated with all types of particles with a volume fraction (10 μg/mL) above Φ_e^*. Typical micrographs are shown in Figure S7. The tubule network is quite similar in all cases, which tends to indicate that the cytoskeleton was not affected significantly by NP internalization and that internalized NPs are not responsible for the slowdown of spreading aggregates.

Above Φ_e^*, NPs are able to glue cells together and to increase W_{CC}.[14] The model developed previously applies equally to cases where NPs are added after the formation of the aggregates or during their formation. For small volume fractions, NPs are internalized and do not remain adsorbed on the membrane of the cells. This regime corresponds to the initial plateau where V^* is not modified. For intermediate volume fractions, NPs saturate the interior of the cells and start to adsorb on the cell surface. In this NP concentration range, V^* decreases. At higher volume fractions, the addition of NPs during formation leads to an even larger decrease in V^*. The slowdown in spreading is more efficient for hybrid cell/NP aggregates. Concerning hybrid cell/NP aggregates, we should consider the volume fraction F during the formation of aggregates (please note that F corresponds to the initial situation in the droplets when cells and NPs are mixed together). Considering an average of 6000 cells per droplet and a cell diameter of 15 μm, we calculated various correspondences between Φ and F for the different NPs (Table S1). It should be noted that the important decrease in spreading velocity at high Φ corresponds to $F = 0.1–0.8$. During the formation of hybrid aggregates, when the total volume of NPs is not negligible it is more difficult to form aggregates because it becomes more difficult for cells to connect to each other and to form a tissue. This may explain why the size of aggregates decreases for this NP concentration regime. The fact that $V^*(\Phi)$ decreases more and more with increasing NP concentration during aggregate formation may also be due to

DOI: 10.1021/acs.langmuir.8b01736
Langmuir 2019, 35, 7396−7404

an increase in the viscosity of aggregates as a result of the excess NPs.

SUMMARY AND CONCLUSIONS

Nanoparticles able to kill cancerous cells in conjunction with an external trigger are well-established tools in nanomedicine. For instance, iron oxide NPs[21,22] and Au NPs[23,24] are used in magnetic hyperthermia and photothermal therapy, respectively. Much attention has been placed on the unintended effects of NPs as a consequence of their physicochemical properties, such as charge and size. Given the complexity of the phenomena that take place between NPs and the biological milieu, this approach has failed to yield general rules.[25] Much less attention has been paid to the ability of NPs to limit cancer propagation by a modification of the mechanical properties of single cells or cell aggregates. We establish here that NPs, intrinsically, can slow the spreading of cell aggregates, often used as tumor models. We interpret our observations on the basis of theoretical tools and models. Interestingly, we demonstrate that the phenomenon occurs with polymer particles over a wide size range and for various surface chemistries. Our different observations suggest that the decrease in aggregate spreading is related to the presence of NPs on the surface of the aggregated cells. The NPs adsorbed on the cell surface act as a glue, increasing the cohesion of the aggregate. Once the surface of the cells is saturated with NPs, the excess NPs incorporated into the aggregates between the cells may increase the aggregate viscosity, which further limits the aggregate spreading velocity. One may surmise that in the clinical setting NPs that reach the vicinity of a cancerous tumor and penetrate it can enhance the cohesion of the tumor by the same mechanism. Such a mode of action of NPs on cancerous tumors merits further study because it can contribute to the reduction of cancer spreading.

ASSOCIATED CONTENT

Supporting Information

The Supporting Information is available free of charge on the ACS Publications website at DOI: 10.1021/acs.langmuir.8b01736.

Details on the theoretical model of the spreading experiment; dynamics of the spreading velocity of aggregates deposited on substrates; cell density in the precursor films of spreading aggregates; PIV of spreading cellular aggregates; viability test with trypan blue of cell aggregates; confocal microscopy of cell aggregates incubated with NPs; confocal microscopy of spreading hybrid cell/NP aggregates; confocal observation of the cytoskeleton of cell aggregates incubated or not incubated with NPs; and correspondence between Φ and F (PDF)

AUTHOR INFORMATION

Corresponding Author

*E-mail: francoise.winnik@helsinki.fi.

ORCID

Françoise M. Winnik: 0000-0001-5844-6687

Notes

The authors declare no competing financial interest.

ACKNOWLEDGMENTS

CT26 cells were a generous gift from Dr. Danijela Vignjevic (UMR 144, Institut Curie, France). This study was supported by the NIMS Molecule & Material Synthesis Platform of the "Nanotechnology Platform Project" and the World Premier International Research Center Initiative (WPI), both operated by the Ministry of Education, Culture, Sports, Science and Technology (MEXT), Japan.

REFERENCES

(1) Quail, D. F.; Joyce, J. A. Microenvironmental Regulation of Tumor Progression and Metastasis. *Nat. Med.* **2013**, *19* (11), 1423−1437.

(2) Arvizo, R. R.; Saha, S.; Wang, E.; Robertson, J. D.; Bhattacharya, R.; Mukherjee, P. Inhibition of Tumor Growth and Metastasis by a Self-Therapeutic Nanoparticle. *Proc. Natl. Acad. Sci. U. S. A.* **2013**, *110* (17), 6700−6705.

(3) Zhou, T.; Yu, M.; Zhang, B.; Wang, L.; Wu, X.; Zhou, H.; Du, Y.; Hao, J.; Tu, Y.; Chen, C.; et al. Inhibition of Cancer Cell Migration by Gold Nanorods: Molecular Mechanisms and Implications for Cancer Therapy. *Adv. Funct. Mater.* **2014**, *24* (44), 6922−6932.

(4) Ali, M. R. K.; Wu, Y.; Ghosh, D.; Do, B. H.; Chen, K.; Dawson, M. R.; Fang, N.; Sulchek, T. A.; El-Sayed, M. A. Nuclear Membrane-Targeted Gold Nanoparticles Inhibit Cancer Cell Migration and Invasion. *ACS Nano* **2017**, *11* (4), 3716−3726.

(5) Yang, J. A.; Phan, H. T.; Vaidya, S.; Murphy, C. J. Nanovacuums: Nanoparticle Uptake and Differential Cellular Migration on a Carpet of Nanoparticles. *Nano Lett.* **2013**, *13* (5), 2295−2302.

(6) Tay, C. Y.; Cai, P.; Setyawati, M. I.; Fang, W.; Tan, L. P.; Hong, C. H. L.; Chen, X.; Leong, D. T. Nanoparticles Strengthen Intracellular Tension and Retard Cellular Migration. *Nano Lett.* **2014**, *14* (1), 83−88.

(7) Zhang, Y.; Hu, L.; Yu, D.; Gao, C. Influence of Silica Particle Internalization on Adhesion and Migration of Human Dermal Fibroblasts. *Biomaterials* **2010**, *31* (32), 8465−8474.

(8) Montel, F.; Delarue, M.; Elgeti, J.; Malaquin, L.; Basan, M.; Risler, T.; Cabane, B.; Vignjevic, D.; Prost, J.; Cappello, G.; et al. Stress Clamp Experiments on Multicellular Tumor Spheroids. *Phys. Rev. Lett.* **2011**, *107* (18), 188102.

(9) Ryan, P. L.; Foty, R. A.; Kohn, J.; Steinberg, M. S. Tissue Spreading on Implantable Substrates Is a Competitive Outcome of Cell-Cell vs. Cell-Substratum Adhesivity. *Proc. Natl. Acad. Sci. U. S. A.* **2001**, *98* (8), 4323−4327.

(10) Steinberg, M. S. Reconstruction of Tissues by Dissociated Cells. *Science (Washington, DC, U. S.)* **1963**, *141* (3579), 401−408.

(11) Saez, A.; Anon, E.; Ghibaudo, M.; du Roure, O.; Di Meglio, J.-M.; Hersen, P.; Silberzan, P.; Buguin, A.; Ladoux, B. Traction Forces Exerted by Epithelial Cell Sheets. *J. Phys.: Condens. Matter* **2010**, *22* (19), 194119.

(12) Trepat, X.; Wasserman, M. R.; Angelini, T. E.; Millet, E.; Weitz, D. A.; Butler, J. P.; Fredberg, J. J. Physical Forces during Collective Cell Migration. *Nat. Phys.* **2009**, *5* (6), 426−430.

(13) Marmottant, P.; Mgharbel, A.; Käfer, J.; Audren, B.; Rieu, J.-P.; Vial, J.-C.; van der Sanden, B.; Marée, A. F. M.; Graner, F.; Delanoë-Ayari, H. The Role of Fluctuations and Stress on the Effective Viscosity of Cell Aggregates. *Proc. Natl. Acad. Sci. U. S. A.* **2009**, *106* (41), 17271−17275.

(14) Brunel, B.; Beaune, G.; Nagarajan, U.; Dufour, S.; Brochard-Wyart, F.; Winnik, F. M. Nanostickers for Cells: A Model Study Using Cell−nanoparticle Hybrid Aggregates. *Soft Matter* **2016**, *12* (38), 7902−7907.

(15) Sveen, J. K. MatPIV. 2006. Available at www.mn.uio.no/math/english/people/aca/jks/matpiv/.

(16) Petitjean, L.; Reffay, M.; Grasland-Mongrain, E.; Poujade, M.; Ladoux, B.; Buguin, A.; Silberzan, P. Velocity Fields in a Collectively Migrating Epithelium. *Biophys. J.* **2010**, *98* (9), 1790−1800.

DOI: 10.1021/acs.langmuir.8b01736
Langmuir 2019, 35, 7396−7404

(17) Moquin, A.; Neibert, K. D.; Maysinger, D.; Winnik, F. M. Quantum Dot Agglomerates in Biological Media and Their Characterization by Asymmetrical Flow Field-Flow Fractionation. *Eur. J. Pharm. Biopharm.* **2015**, *89*, 290−299.
(18) Beaune, G.; Stirbat, T. V.; Khalifat, N.; Cochet-Escartin, O.; Garcia, S.; Gurchenkov, V. V.; Murrell, M. P.; Dufour, S.; Cuvelier, D.; Brochard-Wyart, F. How Cells Flow in the Spreading of Cellular Aggregates. *Proc. Natl. Acad. Sci. U. S. A.* **2014**, *111* (22), 8055−8060.
(19) Vedula, S. R. K.; Leong, M. C.; Lai, T. L.; Hersen, P.; Kabla, A. J.; Lim, C. T.; Ladoux, B. Emerging Modes of Collective Cell Migration Induced by Geometrical Constraints. *Proc. Natl. Acad. Sci. U. S. A.* **2012**, *109* (32), 12974−12979.
(20) Pan, Z.; Lee, W.; Slutsky, L.; Clark, R. a F.; Pernodet, N.; Rafailovich, M. H. Adverse Effects of Titanium Dioxide Nanoparticles on Human Dermal Fibroblasts and How to Protect Cells. *Small* **2009**, *5* (4), 511−520.
(21) Béalle, G.; Di Corato, R.; Kolosnjaj-Tabi, J.; Dupuis, V.; Clément, O.; Gazeau, F.; Wilhelm, C.; Ménager, C. Ultra Magnetic Liposomes for MR Imaging, Targeting, and Hyperthermia. *Langmuir* **2012**, *28* (32), 11834−11842.
(22) Di Corato, R.; Espinosa, A.; Lartigue, L.; Tharaud, M.; Chat, S.; Pellegrino, T.; Ménager, C.; Gazeau, F.; Wilhelm, C. Magnetic Hyperthermia Efficiency in the Cellular Environment for Different Nanoparticle Designs. *Biomaterials* **2014**, *35* (24), 6400−6411.
(23) Van de Broek, B.; Devoogdt, N.; D'Hollander, A.; Gijs, H.-L.; Jans, K.; Lagae, L.; Muyldermans, S.; Maes, G.; Borghs, G. Specific Cell Targeting with Nanobody Conjugated Branched Gold Nanoparticles for Photothermal Therapy. *ACS Nano* **2011**, *5* (6), 4319−4328.
(24) Fazal, S.; Jayasree, A.; Sasidharan, S.; Koyakutty, M.; Nair, S. V.; Menon, D. Green Synthesis of Anisotropic Gold Nanoparticles for Photothermal Therapy of Cancer. *ACS Appl. Mater. Interfaces* **2014**, *6* (11), 8080−8089.
(25) Tay, C. Y.; Setyawati, M. I.; Xie, J.; Parak, W. J.; Leong, D. T. Back to Basics: Exploiting the Innate Physico-chemical Characteristics of Nanomaterials for Biomedical Applications. *Adv. Funct. Mater.* **2014**, *24* (38), 5936−5955.

DOI: 10.1021/acs.langmuir.8b01736
Langmuir 2019, 35, 7396−7404